FLORE
Repository istituzionale dell'Università degli Studi di Firenze

On the use of Gurney Flaps for the aerodynamic performance augmentation of Darrieus wind turbines

(Article begins on next page)

19 October 2024

On the Use of Gurney Flaps for the Aerodynamic Performance Augmentation of Darrieus Wind Turbines

Alessandro BIANCHINI[1a*], Francesco BALDUZZI[1b], Daniele DI ROSA[1c], Giovanni FERRARA[1d]

[1] Department of Industrial Engineering, Università degli Studi di Firenze
Via di Santa Marta 3, 50139, Firenze, Italy
Phone +39 055 275 8773
Fax + 39 055 275 8755

Abstract

Gurney Flaps (GFs) can enhance the aerodynamic performance of airfoils, making them generate more lift and delaying the onset of stall. Since their potential was discovered in the early '70s, GFs have been applied in several fields, including wind turbines. Here, the research has been focused mostly on the use of GFs in Horizontal Axis Wind Turbines (HAWTs), whereas a lack of studies involving the application of these devices on Darrieus Vertical-Axis Wind Turbines (VAWTs) is apparent in the literature. The benefits induced by GFs could actually be particularly interesting for this type of wind turbines, which are presently receiving a renewed attention from the industry.

In the present work, an extended numerical analysis using Computational Fluid Dynamics (CFD) was carried out with the aim of evaluating the potential of using Gurney Flaps for the power augmentation of Darrieus wind turbines.

After a validation of the numerical approach using wind tunnel experimental data on a static airfoil, the simulations have assessed the impact of different GF mounting and height on board airfoils moving in the cycloidal motion typical of Darrieus wind turbines. The results on a single rotating airfoil allowed the analysis to highlight the physical phenomena taking place past the rotating blades, including the delay of stall and the modifications induced on the surrounding flow field; power enhancement higher than 20% were shown for some configurations. Then, impact of GFs on a real three-blade turbine was analysed. The best configuration resulted in a 2%c GF installed in the inner side of the airfoil, so to have a better torque extraction in the downwind half of the revolution. The GF benefits were apparent especially at lower tip-speed ratios, suggesting its use both for newly-designed turbines and even as a retrofitting solution in existing rotors.

Keywords: Darrieus, wind turbine, Gurney Flaps, CFD, power augmentation, flow control

1. Introduction

1.1 Background

The increasing interest in deep-water floating applications and on wind turbine installations in turbulent flows, is putting vertical-axis wind turbines back again in research agendas [1]. Even if

a) alessandro.bianchini@unifi.it (* = corresponding author)   b) francesco.balduzzi@unifi.it

c) daniele.dirosa@unifi.it   d) giovanni.ferrara@unifi.it

horizontal-axis turbines are still by far the most exploited solution, in the two aforementioned fields of application the Darrieus concept seems to offer some undisputed advantages, like the more favorable structural loads, the insensitivity of these rotors on changes in wind direction, misaligned flows or turbulence [2]. Moreover, it should be remembered that the Darrieus concept is intrinsically very suitable also for tidal current applications, where the higher fluid density allows a reduction of the revolution speed, while keeping the advantages of the Darrieus concept in terms of omni-directionality [3-4].

However, the overall energy conversion efficiency of these machines is still lower than that of horizontal-axis ones [5]. To partially fill this gap, innovative aerodynamic solutions are being studied (e.g. [6-7]), together with a continuous research into a deeper understanding of the physics involved in these rotors functioning and of the influence of the operating parameters [8-10]. Another possible way of enhancing the performance of Darrieus rotors could be represented by passive or active flow control devices to be applied on the airfoils [11]. Inter alia, Gurney Flaps (GFs) are one of the most attractive solutions.

Gurney Flaps are simple devices consisting in small tabs that can be applied perpendicularly to the trailing edge of airfoils, on their pressure side, to increase their aerodynamic performance. They were firstly implemented in the early '70s on the rear spoilers of F1 vehicles by the US driver Dan Gurney, who experienced an increase of the downforce thanks to these devices. Later, Liebeck [12] conducted a systematic experimental campaign on a Newman airfoil (a wedge-shaped airfoil with an elliptical leading edge), actually confirming that GFs could enhance the lift force of airfoils. He also suggested that GF height should be kept below 2%c to maximize the aerodynamic benefits, which would be otherwise nullified by a noticeable increase in drag. In his study, Liebeck assumed that the flow field around the airfoil underwent a change that could be theoretically described by the picture reported in Figure 1, where a comparison with the flow over the smooth airfoil is also shown.

This change basically consists in the formation of a stagnation zone upstream of the GF, i.e. a separation bubble characterized by an adverse pressure gradient, and a couple of counter-rotating vortices downstream the GF. Many studies [13-20] later confirmed the presence of this characteristic vorticity, pointing out that it was responsible for an increase of suction on the airfoil upper surface and of pressure on its lower surface, and accordingly for a substantial increase in the lift coefficient. Furthermore, it was found that the aft-loading of the airfoil was augmented and the flow was pushed downwards after it lefts the trailing edge. The same works also highlighted that the stall was achieved at a lower angle of attack in comparison with the baseline smooth airfoil, and the zero-lift angle of attack became more and more negative as the GF height was increased, suggesting that the effective camber of the airfoil was augmented. Lastly, as remarked by several other works [21-24], the deployment of GFs involved also the presence of a von Karman vortex street of alternately shed vortices in the wake of the airfoil.

As one can easily imagine, the effects linked to the use of GFs strongly depend on their configuration, i.e. their geometrical features as well as their mounting details. Among them, the height of the GF is surely one of the pivotal parameters, since the lift enhancing effect of the flap is strengthened as soon as its height is increased. At the same time, the drag force is likewise emphasized, such that its magnitude could nullify the GF benefits if a certain threshold of the flap height is exceeded.

Accordingly, many authors [19,25,26] concur with the fact that the GF size should be kept below the boundary layer thickness measured at the trailing edge on the pressure side of the airfoil, in order to obtain a beneficial lift-to-drag ratio.

1.2 Aim and methods

The GF has proven to have interesting implications in a wide range of fields. The work by Wang et al. [27], as well as that of Troolin [23], indeed provides an extensive overview of the GF applications, which include both low and high-speed airfoils [28], aircrafts, wings, helicopter rotors [29] and, recently, wind turbines. Focusing on this latter application, many literature instances suggest

the GF as a promising device not only for active flow control [30-35], but also for turbine performance increase [36-38]. Notwithstanding this, it's worth remarking that all the aforementioned works coped with the application of GF on HAWTs, whereas the lack of studies concerning the deployment of this device on VAWTs was apparent. Only a few papers were indeed found addressing specifically this issue [39-41], even though the analyses are often based on lumped aerodynamic coefficients, discarding several unsteady aerodynamic phenomena, which are however of capital relevance for a correct description of the GF effects.

The present work thereby is aimed at investigating the effects of GFs on the performance of a Darrieus wind turbine by means of 2D unsteady CFD simulations. In particular, both low (left-hand side of the power coefficient curve) and high (right-hand side of the power coefficient curve) tip-speed ratio (TSR – Eq. 1, where Ω is the revolution speed of the turbine of radius R and U is undisturbed wind speed) were studied. Different GF sizes and mounting configurations were also tested.

$$TSR = \frac{\Omega \cdot R}{U} \tag{1}$$

The study is organized as follows. A detailed presentation of the numerical approaches used in the study is first presented in Section 2, together with the selected study cases. Indeed, a literature case study concerning the use of GFs on a static airfoil was first selected, with the purpose of validating the selected CFD setup by means of experimental findings. The selected case study presented the static polars of a NACA0011 airfoil [15], with and without GFs, obtained with wind tunnel tests. The effects of mounting GFs on a Darrieus turbine were then investigated using both a single NACA0021 airfoil in cycloidal motion and a full turbine featuring the same airfoils. The results related to all these airfoils are reported in Section 3. The results are finally discussed.

2. Methodology

2.1 CFD validation

Before going into the actual investigation about the effects of GF on the Darrieus turbine, a validation of the numerical model used in the following calculations was carried out. In particular, the aim of the study presented in this section, was to verify that CFD was able to predict the trend of the airfoil static polars effectively. If in fact, the approach was proved to be very predictive in case of conventional smooth airfoils [42], its suitability also for those equipped with GFs had to be verified. To this end, the study from Myose et al. [15] was here considered. The authors of [15] performed experimental tests on a NACA0011 airfoil in the Wichita State University Beech memorial low speed wind tunnel. For the purpose of the present study, the data sets corresponding to the smooth airfoil and to GF heights of 1%c and 2%c were considered, since they were fully comparable with the values that will be taken into account in the present study. In the paper, the authors published raw data directly from experiments, but gave full details about the wind tunnel and the experimental setup. In order to compare the results with CFD simulation in an open domain, experimental data were then corrected using the classical expressions for solid blockage and wake blockage into a nearly two-dimensional domain reported in [43].

2.2 Case study and test plan

In order to address the analysis of the GF effect on the Darrieus VAWTs, a case study was first selected. Namely, the 2D model used in CFD calculations was extrapolated from the turbine which has been tested recently in the wind tunnel of the Politecnico di Milano (Italy) by Dossena et al. [44].

127 The same rotor, whose main geometrical features are listed in Table 1, was also exploited in several
128 works by Balduzzi et al., by means of both 2D [45-47] and 3D [48,49] CFD simulations.
129   In particular, most of previous works were focused on the rotational regime corresponding to
130 TSR=3.3, since it was deemed to be particularly interesting within the whole functioning range of the
131 turbine. On one hand, this condition is characterized by a fairly high power coefficient (near to the
132 peak of the power curve) and thus it represents a possible working condition for the rotor; on the other
133 hand, it involves several complex aerodynamic phenomena, including stall, because of the relatively
134 large variation of the incidence angle occurring during a revolution, and thus it poses remarkable
135 challenges in terms of CFD study. Based on this significant amount of past numerical experience
136 concerning the regime of TSR=3.3, this functioning condition was selected as the starting point for
137 the present investigation.
138   According to [50-52], it was also decided not to immediately simulate the complete three-blade
139 rotor, but to initially reproduce a one-blade study turbine having the exact features of the one reported
140 in Table 1. This decision was based both on physical considerations and on hardware limitations. On
141 one side, this strategy indeed allowed the authors to isolate the aerodynamic effect of GFs from the
142 complicated aerodynamic phenomena involved by multiple blade/wake interactions occurring in a
143 real multi-blade rotor. On the other side, from a more practical viewpoint, it also made it possible to
144 mitigate the computational burden associated with the simulations: the need of providing a proper
145 level of spatial refinement in proximity of the blade, would indeed have required a grid with more
146 than 1.5 million elements for a three-blade rotor, which would have taken too much time and exceeded
147 the resources available for the present study. Accordingly, the more affordable computational burden
148 made possible to perform several sensitivity analyses, as better clarified below.
149   In summary, the analysis was developed through three main conceptual steps, detailed below:

150   1. *Assessment of GF effects on NACA0021 static polars*
151   The suitability of the numerical approach in replicating the aerodynamic effect of GFs was
152   first assessed on the static NACA0021, being this the airfoil mounted on the case study
153   rotor; in particular, due to the lack of literature studies concerning the GF effects on this
154   specific airfoil, the static polars using a 2%c GF were calculated and compared to those of
155   the smooth airfoil.

156   2. *GF effects on a single NACA0021 airfoil in Darrieus motion*
157   The functioning point corresponding to TSR=3.3 was studied and a first sensitivity
158   analysis was carried out against different configurations of the GF, keeping its height fixed
159   at a value of 2%c (corresponding to approximately 1.7 mm for the present case study).
160   More in detail, the following configurations of the GF, which differed each other according
161   to the side of the blade where the GF was mounted (see Figure 2), were simulated and
162   compared:
163   ▪ *Baseline smooth* configuration: baseline airfoil with no GF;
164   ▪ *GFin* configuration: flap mounted on the inner side of the airfoil, that is, the one
165   facing the axis of rotation of the turbine;
166   ▪ *GFout* configuration: flap mounted on the blade's outer side, that is, the one facing
167   the boundaries of the computational domain;
168   ▪ *GFboth* configuration: flap mounted on both sides of the airfoil.
169   The reasons why these three different options were chosen for the GF, as well as the
170   corresponding expected outcomes in terms of performance for the wind turbine, will be
171   better clarified in Section 3.3.
172   A sensitivity analysis on different heights of the GF (h_{GF}) was then carried out, in order
173   to assess which size would have been more valuable for the simulations at other TSRs.

174	Hence, in addition to the previously investigated 2%c height, also 3%c ($\approx$2.6 mm) and
175	4%c ($\approx$3.4 mm) sizes were simulated.
176	Finally, the analysis was extended to other functioning points of the hypothetical
177	one-blade rotor, i.e. TSR=2.4, TSR=3.9, TSR=4.5 and TSR=6.0. For each of these values,
178	the size of the GF was kept at 2%c, whereas its mounting configuration was varied within
179	the ones reported above.

181 | 3. *GF effects on the full three-blade case-study Darrieus turbine*

181	The final part of the present study coped with the full three-blade rotor of Table 1. By
182	doing so, the impact of the mutual interaction between the blades could be accounted for.
183	Given the significantly higher computational burden involved, only one GF height was
184	tested (namely, the 3%c GF). The reasons that made the authors select this GF size will be
185	better explained in Section 3.6. The power coefficients at different TSRs were calculated
186	for each of the previous GF configurations, and the power curve associated with each of
187	them was obtained.

2.3 Numerical CFD approach

The computational domains adopted for the CFD simulations are reported in Figure 3. In case of the NACA0011 static polars used for the CFD validation (calculated at $Re = 2.2^{x}10^6$, i.e. the same value declared by the study by Myose et al. [15]), as well as those used for the first preliminary assessment of the GF effect on the NACA0021 static airfoil (calculated at $Re = 1.5^{x}10^5$), the domain was made of the conventional bullet shape (Figure 3(A)), featuring an overall widening angle of 50 deg and distances of 34 and 40 chords upstream and downstream of the airfoil, respectively. The choice of the bullet-shape domain in case of static polars is due to the chance given by this shape of investigating the whole set of angle of attack (AoA) simply modifying the flow angle at the inlet, while keeping the computational grid fixed. To avoid any recirculation in the inlet boundary, of course the maximum AoA is that corresponding to the inclination of the lateral sides of the domain itself. The dimensions of the bullet, were in agreement with the most conservative suggestions that can be found in the literature.

As regards the simulations of the single rotating airfoil, as well as the full three-blade rotor, the sliding mesh technique was employed [53-55]. The physical domain was then split into two subdomains (Figure 3(B)), i.e. a circular zone containing the airfoil, rotating with the same angular velocity of the rotor, and a rectangular fixed outer zone, determining the overall domain extent. In this case, the inlet velocity is always normal to the boundary, then the bullet-shaped domain is not appropriate anymore. The overall characteristics of the computational domain are in agreement with the prescriptions of [55]. Given the purpose of this analysis, only the airfoil was taken into account, neglecting the presence of the spoke and the shaft. According to the sensitivity analyses on this kind of study cases reported in [45-47], a velocity-inlet boundary condition was imposed at the inlet section, which was placed 40 rotor diameters upwind from the rotating axis. To reproduce the experimental data of [44], the inlet wind velocity was set to 9 m/s. The ambient pressure condition was imposed at the outlet boundary, 100 rotor diameters downwind, while a symmetry condition was defined on lateral boundaries, placed at a distance of 30 rotor diameters. The stationary and rotating regions communicate with each other by means of a sliding interface condition [54].

The works by Balduzzi et al. [51,55] were taken as the main references in order to select the most suitable numerical settings for the solver. For the sake of completeness, however, a brief overview on the main settings of the simulation models is given below.

The commercial code ANSYS® FLUENT® [56] was used in the two-dimensional form to solve the time-dependent unsteady Reynolds-Averaged Navier–Stokes (U-RANS) equations in a pressure-based formulation. The fluid was air, modeled as an ideal compressible gas with standard ambient conditions, i.e. a pressure of $1.01^{x}10^5$ Pa and a temperature of 300 K. Based on the comparative

analyses of [55], the turbulence closure was achieved by means of Menter's Shear Stress Transport (SST) model [57], which is derived from the k-ω two-equation formulation and coupled with the Enhanced Wall Treatment for the computation of the boundary layer in the near-wall regions. The *Coupled* algorithm was employed to handle the pressure-velocity coupling. The second order upwind scheme was used for the spatial discretization of the whole set of RANS and turbulence equations, as well as the bounded second order for time differencing to obtain a good resolution.

As regards the static polars, the achievement of convergence was assessed verifying that the difference between two consecutive computed values of the lift and drag coefficients (Eq. 2, where ρ is the air density, S the blade area, W the relative speed, F_L and F_D are the lift and drag forces, respectively) remained constantly below a threshold level of 0.1%:

$$c_L = \frac{F_L}{0.5 \cdot \rho \cdot S \cdot W^2} \qquad c_D = \frac{F_D}{0.5 \cdot \rho \cdot S \cdot W^2} \qquad (2)$$

As regards the rotating airfoil, as well as the full three-blade turbine, the global convergence of each simulation was monitored by considering the difference between the mean values of the torque coefficient (Eq. 3, where A is the turbine front area, U is the absolute wind velocity and R is the turbine radius) over two subsequent revolutions. The periodicity error threshold was set to 0.1%:

$$c_T = \frac{2 \cdot \text{torque}}{\rho \cdot A \cdot U^2 \cdot R} \qquad (3)$$

The meshes generated for the two domains were of unstructured type. Triangular elements were used for the discretization of the core flow region, whereas a structured O-grid was created around the airfoils to accurately resolve the boundary layer.

The first element height was always chosen so as to guarantee that the y^+ values at the grid nodes of the first layer above the blade wall did not exceed the limit of the SST turbulence model, i.e. $y^+ \sim 1$. The expansion ratio for the growth of elements starting from the surface was kept below 1.05 to achieve good mesh quality. The airfoil surface was discretized with a number of nodes which varied between 1000 and 2300, depending on the shape of the simulated airfoil (either NACA0011 or NACA0021), as well as the size of the GF and its configuration.

Proper mesh sensitivity studies were performed for all the study cases. In case of the static polars for both the NACA0011 and the NACA0021 (in case of both the smooth airfoils and the one with GFs), three computational grids were generated by varying the number of nodes on the airfoil surface and the refinement level applied into the wake zone downstream of the GF. The three meshes were featuring a total grid size of approximately 2.3×10^5, 4.3×10^5 and 8.8×10^5 elements, respectively. It was found a difference between the lift coefficients predicted by the two most refined meshes constantly lower than 1%. In case of rotating airfoils, the meshes were verified by proper mesh sensitivity studies in [48,49]. In case of the use of GFs, the same maximum level of refinement used for the static case for the NACA0021 was used. Overall, it was verified after the simulations that the meshes for the rotating airfoils were able to fulfill the requirements in terms of limiting the dimensionless vorticity proposed by Balduzzi et al. [51]. Figure 4 shows some details of the computational grid used for the simulations of the rotating airfoil, with particular focus on the refinement zones used to properly discretize the leading and trailing edges of the airfoil and its wake. As an example, the *GFboth* configuration is reported there.

Regarding the temporal discretization, the static polars were calculated using a steady RANS approach up to the static stall angle, while after that the method was switched to a U-RANS one, with a timestep of $5^{\times}10^{-4}$ s and $2^{\times}10^{-3}$ s for the NACA0011 and the NACA0021, respectively. In case of the rotating blade, as well as the complete rotor, additional care in comparison to conventional Darrieus simulations was requested by the selection of the angular spacing between two consecutive timesteps (angular timestep). Firstly, this had to be proportionally adapted to the revolution speed of the rotor, i.e. it had to be reduced for small TSRs, in order to match the requirements in terms of limiting the

266 Courant number in proximity of the blades as proposed by Balduzzi et al. [51,55]. Moreover, in the
267 present application, the presence of the shedding vortices generated by the flow over the GF could
268 not be disregarded, because a too coarse temporal discretization could prevent the phenomenon itself
269 from being detected.
270   Accordingly, the pressure fluctuations associated with the shedding would not be captured by the
271 CFD and this could potentially lead to a wrong prediction of the torque and power curves.
272 Consequently, a maximum threshold for the value of the angular timestep was established in order to
273 ensure that at least 10 points per shedding cycle were captured by the simulations. More in detail, the
274 angular sector corresponding to a shedding cycle was calculated by Eq. 4, where f_s was the expected
275 shedding frequency and was evaluated in Eq. 5, according to the definition of the Strouhal number
276 (St).

$$\Delta\vartheta_S = \frac{\Omega}{f_S}\frac{180}{\pi}$$

(4)

$$f_S = St\frac{W_{max}}{h_{GF}}$$

(5)

277   In the previous equation, $W_{max}=(U^2+\Omega R^2)^{0.5}$ is the highest relative velocity experienced by the
278 airfoil and h_{GF} is assumed to be the characteristic length governing the shedding development. After
279 each simulation, the consistency of the selected timestep was verified using the actual shedding
280 frequency detected by the simulations. As a result, timestep sizes ranging between 0.08 deg and 0.72
281 deg were used. The size of the different computational grids and the calculations cost are reported in
282 Table 2.
283   As a final remark on the numerical CFD approach, it is worth pointing out that, in spite of the
284 increase of the computational cost, the authors decided to simulate even the single airfoil in a real
285 cycloidal motion (i.e. with the blade rotating physically in a straight flow field), rather than in an
286 equivalent pitching motion, in order not to discard the mutual interaction between the blades (e.g. due
287 to vortices detached upwind and convected by the flow). Moreover, this allowed also to account for
288 the AoA variation downwind due to the reduced wind speed.

3. Results and discussion

289

3.1 Validation

290

291   The comparison between the experimental polars of the NACA0011 obtained experimentally by
292 Myose et al. [15] and those resulted from the CFD simulations of the present study is reported in
293 Figure 5. Impressive agreement was found between the two data sets. The behavior of the smooth
294 NACA0011 airfoil was perfectly described by CFD, which also captured exactly the static stall angle.
295 A very slight overestimation of the post-stall lift (and under-estimation of the post-stall drag) was
296 only noticed. Most of all, CFD simulations were able to correctly reproduce the effect of the Gurney
297 Flaps, both for the 1% and the 2% chord height. The only minor discrepancy was a less abrupt stall
298 for the 2%c case. Overall, the agreement was considered fully satisfactory, thus corroborating the
299 suitability of the CFD approach.

3.2 Preliminary assessment of GF effects on NACA0021 static polars

300

301   Figure 6 reports the calculated lift and drag coefficients of the NACA0021, both for the baseline
302 smooth and the *GFin* configurations. For the latter, a h_{GF} of 2%c was selected.

Please note that, due to the complicated flow structures originated in correspondence to the GF, the simulations of this configuration required a much more refined angular discretization of the polar with respect to the smooth airfoil; markers for the GF curve were not reported for readability. The results were in good agreement with expectations. In particular, an enhancement is apparent in the lift curve of the NACA0021 with the GF, whose peak value was increased by 58% in comparison with the baseline configuration. The angle of attack corresponding to this peak turns out to be mildly affected by the GF, having a value of roughly 12° in both cases. The effective camber augmentation is likewise apparent from Figure 6, since a positive C_L is obtained for the zero incidence in case of the NACA0021 with the flap. It is also interesting to note that the lift-enhancing effect of the GF increases as the AoA is raised within the pre-stall region, leading to a steeper trend for the modified airfoil. The stall occurs right after the highest C_L for the smooth airfoil, i.e. at an AoA of 13°. A small decrease of the C_L is instead clearly outlined for the airfoil with the GF up to 15°, where a narrow zone of instability anticipates the abrupt onset of stall at an AoA of 16°. According to [19], this kind of stall may be induced by a sudden leading-edge bubble burst, rather than a progressive separation starting from the rear region of the airfoil. Besides, the stall of the airfoil with the GF is coupled with a sharp rise of the C_D, which - as expected - is higher than that of the smooth airfoil, particularly after the arising of stall.

3.3 Sensitivity analysis on the GF configuration

Some preliminary considerations can be made on the effects achievable by adding the GF with different configurations on the airfoil, simply based on the study of the velocity triangles obtained during revolution of the turbine. According to the inherent functioning principle of the Darrieus turbine, each side of the blade acts alternatively as pressure side (PS) or suction side (SS), depending on whether the blade itself is passing through the upwind or the downwind zone. Namely, the outer side of the blade acts as PS in the upwind half of the revolution, whereas it acts as SS in the downwind one. Conversely, the opposite happens for the inner side of the blade. Provided that the GF exhibits its benefits within a restricted range of positive incidence angles, its effects might be expected to be favorable only within narrow portions of the revolution, whereas they might be mild, or even detrimental, within others. Broadly speaking, the *GFin* and *GFout* configurations were likely to enhance the lift on the airfoil, and hence the power extraction, only within the downwind and the upwind zone, respectively, i.e. where the relative velocity incidence and the GF position matched favorably. On the other hand, the *GFboth* configuration was expected to give an overall in-between result, since reasonably it would have taken the benefits of both the cases above, introducing however a higher drag force due to the larger size of the flap. These theoretical expectations were confirmed by the results at TSR=3.3 of Figure 7, where the torque coefficient profiles for each configuration are reported.

As expected, when the GF is mounted on the inner side of the blade, it provides approximately the same energy extraction of the smooth airfoil in the upwind zone, whereas it significantly enhances the torque in the downwind one, leading to an increase of $c_{T,ave}$ of 23.3% in comparison with the baseline smooth configuration. On the other hand, when the GF is located on the outer side of the airfoil, it leads great benefit in the upwind zone, while the performances in the downwind zone are mildly worsened in comparison to the baseline configuration. The increase of the $c_{T,ave}$ is of 23.6% in this case, i.e. very close to the value associated with the previous situation: interestingly, the enhancement led by the *GFin* configuration within the downwind zone and the one provided by the *GFout* configuration in the upwind region are of the same order of magnitude, resulting in basically the same energy extraction even if this is obtained with completely different torque profiles over the revolution.

Focusing now on the *GFboth* configuration, it is apparent that the envisaged outcomes were correct in this case, too. In particular, the resulting torque profile is affected by both the advantages and disadvantages of both the *GFin* and *GFout* configurations. This is proven by the fact that its trend seems to be reasonably well predictable on the basis of the torque profile of the baseline smooth

airfoil, adding up to it the positive or negative contributions deriving by both the *GFin* and the *GFout* configurations, for each of the azimuthal positions. Notwithstanding this, it is also apparent that the final profile may be affected by other non-linear effects which clearly make the actual result deflect from this mere algebra procedure. However, what matters is that apparently the advantages overcome the disadvantages, resulting in a 35.3% increase in the $c_{T,ave}$.

3.4 Sensitivity analysis on the GF height

In order to contain the calculation burden, only one GF configuration was selected for the sensitivity analysis on h_{GF}. Namely, provided that the *GFboth* configuration was showed to guarantee the best results through the previous Section 3.3, it was deemed to be also the most reasonable choice for the investigation described below.

From a perusal of Figure 8, where the torque profiles obtained for different h_{GF} are reported, some observations can be done. First, increasing h_{GF} from 2%c to 3%c did not bring any additional performance improvement in terms of average torque over a revolution: the $c_{T,ave}$ increases by 35.7% in comparison with the baseline smooth air-foil, which is basically the same value provided by the 2%c flap. Apparently, although a slight growth of the torque is noticeable for ϑ ranging approximately from 75° to 180°, this is then nullified by the mildly poorer performance occurring in the whole downwind region, as well as within the first 70° sector of the upwind half of the revolution. Second, it's readily apparent that a further increment of h_{GF} from 3%c to 4%c is totally detrimental for the performance of the turbine. In fact, besides the fact that the $c_{T,ave}$ is mildly worsened in comparison with the smooth airfoil (-5.7%), a large portion of the revolution is clearly affected by pretty strong oscillations of the torque coefficient: this is distinctly an indication of the presence of shedding vortices within the flow field interacting with the blade. These fluctuations seem to onset for a ϑ between 270° and 300°, and they persist until the blade reaches the 90° position, achieving their highest amplitude between 0° and 20°-30°. The energy extraction of the turbine is seriously penalized by this phenomenon, which gives rise to a steep drop of the torque coefficient since the very beginning of the shedding, leading the c_T to become even negative from approximately 325° to 45°. One may question why the shedding arises precisely when the 4%c flap is mounted on the blade, whereas no such issue was found for the 2%c and the 3%c flaps.

This can be explained taking into consideration the physics underlying the functioning of the Darrieus turbines: the larger the upwind torque extraction, the lower the energy content within the downwind flow, which results in a smaller absolute wind speed acting on the blade in that region and hence in a smaller incidence of the relative velocity on the airfoil.

In this specific case, a smaller angle of attack of the flow over the airfoil with the GF is deemed to further promote the shedding, since the flow tends to interact more and more perpendicularly towards the flap itself as the incidence tends to zero. Accordingly, the 4%c GF, providing the highest peak torque within the upwind region among the investigated h_{GF}, is therefore deemed to lead to the most conducive situation in terms of shedding promotion. Conversely, the 2%c and 3%c flaps involve a smaller upwind energy extraction, resulting in a downwind incidence which is high enough to prevent shedding developing: the flow is indeed assumed to generate a thicker boundary layer or even separate on the suction side of the airfoil, leading to an asymmetrical interaction with the GF and thus hampering the generation of organized vortex structures.

Finally, it is interesting to note that the increase of h_{GF} produces two effects: first, the torque peak becomes higher, and second, it is achieved later during the revolution. This is likely due to the combination of different factors. On one hand, the lift enhancement effect of the GF becomes stronger as its height is increased, thereby the blade is capable of extracting additional energy even for incidence conditions which would already become unfavorable for the baseline smooth airfoil. Namely, the torque coefficient begins to decrease just after $\vartheta \approx 87.8°$ for the latter, whereas it is still increasing there for the GF-airfoils: in particular, the peak c_T of the 4%c airfoil is achieved for an azimuthal position of $\vartheta \approx 94.4°$. On the other hand, as the h_{GF} is increased, so does the drag force, and this is particularly apparent in the first 30° range of the upwind region: here, the flow incidence is

almost null, hence the GF has the only effect of exacerbating the drag force, leading to a poor performance. Accordingly, the beginning of positive torque production is delayed, shifting the whole trend to the right. This is especially noticeable for the 4%c case, for which the situation is further worsened by the presence of shedding, as discussed above. In fact, despite of the highest slope of this curve, due to the greatest boost action of the GF, the torque turns positive only after $\vartheta \approx 45$ deg. Subsequently, it quickly achieves its top value and then it cannot be any longer risen, since the airfoil has already reached an adverse azimuthal position, where the enhancing effect of the GF cannot outweigh the fact that the airfoil begins to stall, no matter of how long the GF itself is.

3.5 Sensitivity analysis on TSR and power curves prediction

Figure 9 reports the power coefficient (Eq. 6) of the various GF configurations as a function of the TSR; the reference power curve for the hypothetical 1-blade turbine provided by [49] and based on a state-of-the-art, free-wake, lifting-line method embedded in open source code QBlade [58] is also displayed as a reference. The importance of analyzing multiple TSRs is due to the fact that the operating conditions (in terms of AoA range and rate of variation during a revolution) deriving from these TSRs are notably different, thus allowing an in depth assessment of the aerodynamic impact of GFs under such variable conditions.

$$c_P = \frac{\text{power}}{0.5 \cdot \rho \cdot A \cdot U^3} \tag{6}$$

Focusing on the results obtained for TSR=3.3 (functioning condition near to the peak, but still in the lift-hand side of the curve, where stall is like to happen), it is readily noticeable that the values of the c_P reflect the observations reported in Section 3.3. The percentage c_P enhancements of each GF configuration in comparison with the baseline are logically the same values therein reported in terms of $c_{T,ave}$. For the reasons explained in Section 3.3, the highest performance improvement in comparison with the baseline case is provided by the *GFboth* configuration, whereas the *GFin* and *GFout* arrangements turn out to be equivalent to each other.

A similar situation is observable at the lowest simulated regime of TSR=2.4, the *GFboth* deployment still proving to be the most effective solution with a 62.5% enhancement of the c_p. Again, the *GFin* and *GFout* arrangements are represented by almost superimposed points, which namely correspond to a 31.3% and 39.1% raise of the c_p. The larger impact of GFs at this TSR can be related to the fact that the AoA range at this TSR is wider than that at TSR=3.3, magnifying the benefits offered by GF in increasing the maximum lift and delaying stall. In particular, a delay of stall in the upwind region at low TSRs is expected to modify remarkably the onset of dynamic stall [48].

Moving forward to TSR=3.9 (i.e. the curve peak, with smaller AoA variation), it is apparent that this regime roughly maximizes the performance of all the three GF configurations. To be more specific, the *GFboth* arrangement seems to show already a very slight decreasing trend, hence its actual peak value may reasonably be assumed to occur just below the TSR=3.9. Conversely, the CFD points corresponding to the *GFin* and *GFout* deployments look to have matched the peak value more accurately. It is curious that the *GFboth* and *GFout* arrangements led in this case to the same 17.3% increment of the averaged power coefficient, which turned out to be 0.370. The *GFin* configuration provides instead c_{P_ave} of 0.360, which raised by 14.6% in comparison with the smooth airfoil.

Another interesting issue occurs at TSR=4.5 (i.e. a condition with an even narrower AoA range), where the *GFboth* configuration shows a notably decreasing slope and it results in the exact power extraction provided also by the baseline smooth airfoil. By the way, this functioning point can be regarded as the one which maximizes the performance of the smooth airfoil, with a c_{P_ave} of 0.328. As regards the *GFin* and *GFout* configurations, they tend to give more or less the same c_P, which is increased by 8% and 10% in the two cases, respectively.

As regards the regime of TSR=6.0, the most evident fact is that the *GFboth* configuration makes the c_P dramatically drop down to a negative value, which implies that the turbine is producing a

449 resistant torque there, rather than extracting energy from the wind: this case is indeed characterized
450 by a 122.5% lower c_P in comparison with the smooth airfoil. On the other hand, the *GFin* and *GFout*
451 configurations still keep ensuring higher efficiency than the baseline case, leading to an enhancement
452 of the c_P of 24% and 20%, respectively.

453   In summary, two main issues arise from the considerations above. The first is that the deployment
454 of the GF on the turbine has the effect of shifting its peak power extraction capability backwards to
455 lower TSRs, in comparison with the case where the baseline smooth airfoil is used. Secondly, among
456 the examined GF configurations, the one featuring the flap mounted on both sides of the blade showed
457 its highest effectiveness at the lowest simulated TSRs, whereas its performance was massively
458 worsened at high TSRs. On the other hand, the *GFin* and *GFout* arrangements brought slightly poorer
459 performance at low TSRs, but constantly provided a better behaviour when compared with the
460 baseline smooth airfoil, including the high-TSR regimes where the *GFboth* configuration was proven
461 to be totally detrimental. Accordingly, this different behaviour turned out to draw up an overall flatter
462 power curve in comparison with the *GFboth* case, which instead would give rise to a very steep trend.
463 Such a selective functioning curve would involve serious handling problems within the rotational
464 speed control, eventually making the rotor less cost-attractive.

465   To understand better the physical reasons underlying the obtained outcomes in terms of c_P, a
466 detailed analysis of the torque coefficient as a function of the azimuthal position of the blade was
467 carried out for each of the investigated TSR regimes. Provided that the torque coefficient trend
468 corresponding to TSR=3.3 has already been discussed in Section 3.3, it was thereby omitted from the
469 comments below.

470   Figure 10 reports the torque profiles corresponding to TSR=2.4. As one can readily notice, a large
471 unsteadiness characterizes the whole torque extraction, which is a typical issue for functioning
472 regimes corresponding to very low TSRs: broad fluctuations are indeed visible within the c_T profiles,
473 regardless of the GF configuration, as a result of the large AoA variations. By a closer examination,
474 it is possible to observe that in the first 90°-100° of the revolution, the baseline and *GFin* curves
475 basically overlap each other, and the same thing occurs between the *GFout* and *GFboth* trends. From
476 that point on, the profiles begin diverging one from another, consistently with the fact that the airfoil
477 starts to experience deep stall conditions: the produced torque drops to negative values, and its trend
478 depicts a number of pretty much pronounced and staggered bumps, depending on which airfoil
479 configuration is considered, as far as the azimuthal position of $\vartheta = 180°$ is reached, with a null torque
480 extraction for all the four cases. The first part of the downwind profile, as long as the position of
481 240°-250°, is characterized by a moderate positive torque production, since the upwind extraction has
482 lowered the energy content of the incoming flow. Subsequently, a second conspicuous drop of c_T
483 occurs, which is nothing but a consequence of the vortex structures which have previously detached
484 from the stalled airfoil within the 100°-180° range and have been conveyed downstream, eventually
485 intercepting the blade itself.

486   Moving forward to the higher simulated TSRs, Figure 11 reports the torque profiles corresponding
487 to the TSRs of 3.9, 4.5 and 6.0. As discussed, these functioning conditions are expected to be
488 characterized by progressively narrower AoA ranges, thus the impact of GFs was attended to be
489 progressively reduced, or even detrimental in some cases due to the additional drag. Concerning the
490 TSR=3.9, and referring to what has previously been commented about the c_P values reported in Figure
491 9, the fact that the *GFboth* and *GFout* configurations give rise to the same c_P is easily understandable
492 from Figure 11: in fact, whilst the former provides a slightly poorer performance between 0° and
493 120°, so does the latter from 210° to 360°, resulting exactly in the same mean c_P. However, a little c_T
494 oscillation is actually observable within the first 45° of the upwind region, for the *GFboth*
495 configuration. This is a signal that vortex shedding, even if at a mild intensity, is beginning to develop
496 within the wake of that airfoil. Furthermore, the higher c_T achieved in the downwind region by the
497 *GFin* arrangement is due to the favourable matching between the GF position and the angles of
498 incidence experienced by the airfoil, as already explained in Section 3.3 for the case of TSR=3.3.

Focusing now on TSR=4.5, one can firstly appreciate that its corresponding torque profiles are by far similar to the previous TSR, especially within the upwind part of the revolution. An equalization between the *GFboth* and the baseline smooth configurations occurs this time, in every way similar to what previously occurred for the *GFboth* and *GFout* cases. The same occurrence happens for the *GFin* and *GFout* arrangements, too. What matters more at this TSR, however, is that the onset of vortex shedding is clearly visible this time over the final portion of the downwind half and the beginning of the upwind one for the torque profile corresponding to the *GFboth* configuration.

Finally, the reason why the *GFboth* configuration involves such a poor power extraction at TSR=6.0 (i.e. the one with the narrowest AoA range) is readily understandable from Figure 11. A massive presence of vortex shedding is indeed clearly visible over most of the downwind half and the beginning of the upwind one for the torque profile corresponding to this configuration. As one can conclude from the discussion provided in Section 3.4 for the 4%c flap, this is indeed the worst situation in terms of shedding promotion: in fact, despite the smaller GF, the TSR is now increased, hence the angle of attack over the airfoil is averagely decreased and eventually the 2%c flap becomes big enough to make shedding vortices arise. By the way, looking closely to the last 70 degrees of the downwind torque profile of the *GFout* configuration, it is possible to identify a barely outlined oscillation of the c_T: this means that not even this GF arrangement is able to totally prevent the onset of vortex shedding, because of the excessive energy extraction within the upwind region of the revolution.

These observations are confirmed by Figure 12, where the contours of the dimensionless vorticity are reported for the four analyzed airfoil configurations at the azimuthal position of 312 deg. As a further evidence, Figure 13 provides the pressure coefficient distribution on the airfoil, for the same azimuthal position. As apparent, the *GFin* configuration turns out to be the only one that allows a torque enhancement without involving the onset of the aforementioned shedding instabilities.

3.6 GF effects on the full three-blade case-study Darrieus turbine

Once the prospects of GFs for power enhancement of blades in cycloidal motion were assessed on the single-blade study cases, their effect on a real 3-blade turbine was evaluated. In this case, the mutual interaction of the blades and their wakes was indeed accounted for.

Before going into the discussion reported below, it is worth explaining why the 3%c size was considered the most reasonable choice for the simulations in case of the full 3-blade rotor. This value was indeed though to represent a good compromise between two requirements. On one side, a higher flap might have been excessive, probably inducing vortex shedding within the wake of the airfoil and worsening the performance of the turbine. On the other, the 2%c flap would have brought no appreciable effects: in fact, the interference effect of the upwind region of the revolution on the downwind one is significantly magnified for the full three-blade rotor, in comparison with the single rotating airfoil of the previous Sections. Consequently, the boosting effect of the GF could not have been detected.

Figure 14 provides the power coefficient trends corresponding to the four compared configurations. Please note that the curve of the baseline smooth configuration was reproduced from [30], where the same case-study rotor was studied. Provided that the peak value of the power coefficient therein occurred for TSR=2.64, this was the first investigated functioning regime.

From a perusal of Figure 14, it is first apparent that the *GFboth* arrangement gives rise to a dramatic worsening of the performance at TSR=2.64, with a drop of -27.2% in comparison with the baseline smooth configuration. On the other side, the *GFin* solution results in a 3.7% enhancement of the power coefficient, while the *GFout* arrangement produces only a very mild decrease of it (-1.5%).

The second set of simulations was run at TSR=2.4. The outcomes revealed that both the *GFin* and *GFboth* configurations led to a significant power extraction improvement, which was of 21.3% and 17.4%, respectively. Again, the *GFout* solution resulted instead in basically no appreciable variation in comparison with the baseline smooth case.

549 As regards the TSR of 2.1, it's interesting to note the 52.6% power increase brought by the *GFboth*
550 configuration, as this could be beneficial for the start-up of the turbine (even if this advantage would
551 be nullified by the subsequent performance drop after TSR=2.4).
552 Moving rightwards to the stable half of the curve, it's apparent that the addition of the GF brings
553 now a decline of the performance, both in the *GFin* and in the *GFout* case. In particular, at the highest
554 simulated TSR (namely, TSR=4.04), a -81% variation is involved by the *GFin* solution, in
555 comparison with the baseline arrangement. It's interesting to highlight that this trend is now reversed
556 in comparison with the single rotating airfoil featuring the *GFin* or *GFout* configurations, which
557 instead provided a better performance at high TSRs in comparison with the baseline smooth
558 configuration (see Figure 9). Furthermore, whereas in that case (single airfoil) the *GFin* and *GFout*
559 solutions gave almost the same results for all the TSRs, here the *GFout* configuration constantly
560 generates lower power coefficients in comparison with the *GFin* solution.
561 To better understand the physical reasons which had led to these results, a detailed analysis of the
562 torque profiles corresponding to each TSR was carried out. Please note that the discussion reported
563 below refers to the torque extraction of a single blade among the three belonging to the full rotor: the
564 complete profile may be derived simply summing the contributions of the three blades, bearing in
565 mind that they are shifted by 120° from each other.
566 Figure 15 reports the torque profiles over the complete revolution at TSR=2.4 and TSR=2.64. It's
567 therein clarified why the *GFin* and *GFboth* configurations lead to a power production augmentation
568 in comparison with the baseline smooth case. This is particularly apparent at TSR=2.4, where the
569 power extraction provided by the unmodified rotor is quite poor. The torque profile corresponding to
570 the baseline case is indeed characterized by an unstable trend, with a negative torque coefficient
571 between 350° and 30°, as well as between 125° and 180°. The boosting effect of the *GFin*
572 arrangement is instead evident: despite a mildly poorer performance between 15° and 95°, it provides
573 a higher efficiency for the remaining portion of the upwind half, and, more importantly, it ensures an
574 excellent behaviour through the whole downwind region, with a nearly flat trend between 210° and
575 340°. The *GFboth* configuration also provides a good performance, even if this is due different
576 reasons. In fact, the torque remains negative until the position $\vartheta = 40°$, afterward it turns positive and
577 increases steeply to reach a very high peak, corresponding to $\vartheta = 90°$. The remaining part of the
578 upwind zone is then characterized by a constantly higher torque extraction in comparison with the
579 other two configurations, at least until $\vartheta = 170°$. Subsequently, the downwind half looks to provide a
580 power production which is slightly lower than the one of the baseline configuration: this is likely due
581 both to the large energy amount which has already been extracted upwind, and also to the outer
582 portion of the GF, which matches improperly with the relative speed direction and nullifies the
583 benefits of the inner portion. The latter issue even more applies to the *GFout* case, whose downwind
584 performance is always the worst among the other configurations, both at TSR=2.4 and TSR=2.64. In
585 particular, when this solution is compared to the baseline smooth case, it shows a significantly higher
586 efficiency within the upwind half, though this is then entirely outweighed by the lower downwind
587 power extraction, resulting in no net advantage. It's also interesting to compare the performance of
588 the *GFout* configuration with the one provided by the *GFin* solution. In fact, the situation is reversed
589 for the latter, as its upwind power production is lower than the baseline rotor, whereas the GF boosts
590 it downwind. When the hypothetical one-blade rotor was tested, this resulted in an equivalent average
591 performance in comparison with the *GFout* case (see Section 3.5), but the same thing doesn't happen
592 now. This can be justified by the stronger interference effect produced by the three-bladed rotor in
593 comparison with the single rotating airfoil: this issue is even more magnified by the *GFout*
594 configuration, which involves practically no flow incidence on the airfoils in the downwind portion.
595 Apparently, this fact penalises the overall performance more than the *GFin* does within the upwind
596 half of the revolution.
597 Moving forward to TSR=2.64, a more stable behaviour is apparent there for the baseline smooth
598 configuration, with a conspicuous reduction of the negative torque region which occurred at TSR=2.4
599 between 125° and 180°. Furthermore, a higher performance is apparent through the entire second half

of the upwind zone, resulting in an average larger power extraction over the whole revolution. Similar considerations apply also to the *GFin* configuration, even if the torque profile corresponding to it turns out to be not so modified in comparison to the one of TSR=2.4. A substantial change occurs instead for the torque profile involved by the *GFboth* configuration, which explains the abrupt drop of the power coefficient reported in Figure 14. Despite this arrangement still provides the highest peak torque in the upwind region, a very poor performance characterizes the whole downwind half: but, more importantly, evident fluctuations appear within the torque profile, starting from $\vartheta = 230°$ and continuing until the position $\vartheta = 45°$. By the way, the onset of these instabilities could be expected, since they had already arisen in the first 40° of the upwind half of the same torque profile, at TSR=2.4. These oscillations, which are due to the presence of strong vortices shedding from the rotating airfoil, are detrimental for the torque extraction, whose curve is heavily shifted downwards.

Figure 16 reports a comparison between the torque profiles produced by the different tested airfoil configurations at TSR=2.1, 3.3 and 4.04. As expected, because of the high irregularity which affects the flow field at low TSRs, the torque profile corresponding to TSR=2.1 is characterized by continuous oscillations between positive and negative values. As discussed in previous studies (e.g. [59]), this is due to the fact that, at low TSRs, the AoA variation is so large to let the airfoil experiencing deep stall, with massive drop of performance and the detachment of macro-vortices that are detached from the blades and then convected downwind by the flow. The interaction of these vortices with the downwind blades contributes to the high variability of the torque profile: for this reason, the effect of the GF doesn't stand out clearly at this rotating regime, and it did not make sense to carry out a specific discussion about that.

Conversely, the higher TSRs involve a much more regular curve, with a positive upwind peak followed by a downwind flat trend. Accordingly, the GF effect is much better outlined at these functioning regimes. Consistently with the poorer performance depicted in Figure 16, the modification induced by the GF at TSR=3.3 is slightly disadvantageous as a whole, both in the *GFin* and the *GFout* case. In fact, despite the former ensures a mildly better performance within the entire downwind zone, not the same occurrence is visible in the upwind half: after just 20°, the torque profile of the *GFin* configuration drops under the one of the baseline smooth case, staying below it for the whole upwind portion of the revolution. On the other hand, as usual, the *GFout* arrangement overly boosts the upwind extraction, which is then paid with a resistant torque all along the downwind half. Furthermore, the latter is also characterized by fluctuations due to the onset of vortex shedding.

Moving forward to TSR=4.04, the reason underlying the bad performance emerging from Figure 16 is readily apparent. The torque profile is indeed greatly shifted downwards, ensuring positive torques only between 60° and 145°. But, what matters more, noticeable oscillations affect the entire torque extraction, revealing that intense shedding vortices are constantly detaching from the blades during their revolution.

4. Conclusions

The possible benefits deriving from the application of Gurney Flaps on the blades of a Darrieus VAWT were investigated within the present work. These devices were in fact thought to represent a simple and effective way to enhance the power extraction capability of those machines (even in a retrofitting strategy), which are experiencing a renewed interest within the wind energy market and research.

To properly capture the unsteady aerodynamics, unsteady CFD simulations were needed. Based on previous experience, 2D simulations were thought to represent the best compromise between accuracy and computational cost. Notwithstanding this, the overall computational burden turned out anyway to be significantly high, since a full-unsteady approach, with heavy spatial and temporal refinement levels, was needed to ensure reliable results.

The numerical setup used for the analyses was first validated with experimental data, in order to verify that it was able to guarantee an accurate description of the effects of GFs on the aerodynamic behavior of the airfoils. Accordingly, a literature case study was selected, concerning the comparison between the static polars of a NACA0011 airfoil with and without GFs. The airfoil polars were reproduced by means of CFD calculations, and the results showed satisfactory agreement with the reference trends, although some discrepancies were found on the static stall angle predicted by CFD.

Subsequently, the effects of mounting GFs on a Darrieus turbine were evaluated. The experimental case study, which was selected for the analyses, featured a three-blade H-Darrieus equipped with a NACA0021 airfoil. A preliminary assessment of the effect of 2%c GF on the static polars of this airfoil was carried out, reproducing the same chord Reynolds number experienced by the airfoil during the rotation. The results showed a notable enhancement of the aerodynamic performance of the airfoil, whose peak lift coefficient was increased by 58% in comparison with its baseline configuration. Furthermore, the whole lift curve was strongly shifted upwards, whereas the drag coefficient turned out to be not significantly modified. The static stall angle looked to be only mildly affected by the application of the GF, remaining around 12°.

Moving forward from these encouraging results, the effects of the GF were first simulated considering a hypothetical one-blade Darrieus having the exact features of the case study rotor: this allowed to focus on the aerodynamic modifications induced by the GF, without any spurious effect deriving from the multiple blade/wake interactions occurring in a real rotor. Furthermore, thanks to the lighter computational burden, several sensitivity analyses were carried out. First, the functioning regime corresponding to TSR=3.3 was analyzed, and three different mounting configurations were compared, featuring a 2%c GF on the inner, on the outer and on both of the sides of the rotating airfoil. Furthermore, the effect of different sizes of the GF on the power extraction capability of the blade was investigated, focusing the analysis only on the latter of the previous three GF configurations and varying its height among 2%c, 3%c and 4%c. Finally, the research was extended to other functioning regimes of the turbine: for each of them, a 2%c GF was tested within the configurations reported above, with the aim of predicting the trend of the power curves. For each of the study cases, the performance of the airfoil was compared with its baseline smooth configuration, paying particular attention to the different torque profiles over the complete revolution.

The results showed that, if the proper GF configuration is selected, it can provide a notable increase of the aerodynamic performance especially at medium-low TSRs. More in detail, when the 2%c GF was applied on the inner side of the airfoil, it was proven to guarantee a 23.1% and 14.6% increase of the power coefficient at TSR=3.3 and TSR=3.9, respectively. Moreover, this GF arrangement avoided the onset of vortex shedding at high-TSR rotating regimes, which instead was promoted when the flap was mounted on the outer or on both sides of the airfoils. Besides, when the GF was mounted on the inner of the blade, it provided also a flatter power curve trend with a lower peak TSR in comparison with the baseline configuration, involving interesting implications for the turbine control.

As a conclusion of the study, the GF effects were evaluated on the real three-blade case study rotor, in order to achieve some preliminary results for further research. A 3%c GF was applied on the airfoils and the same previous GF configurations were compared. Very promising results were found: the power coefficient was increased by 21.3% at TSR=2.4, when the GF was applied on the inner side of the airfoils.

The results actually showed that GFs entail the potential of ensuring significant improvements for the energy yield capability of VAWTs. Although these results can be considered pretty innovative, further research is surely needed in order to better assess the benefits of GFs for Darrieus turbines. For example, the implementation of these flaps implies additional material needed for the construction of the machine, with an increase in the drag force experienced by the blades: this unavoidably has an impact on the structural stresses the struts have to bear.

Future analyses will investigate different rotor geometries, airfoils and turbine dimensions. Moreover, many other configurations of the GF could be considered and compared: among them,

698 flaps with a tilt angle with respect to the chord of the airfoil, as well as pivoting GFs (which could
699 switch their position when the blade moves from the upwind to the downwind region), represent only
700 a few examples of the numerous studies that could be performed in the future.

5. Nomenclature

702
703   Acronyms
704   AoA   Angle of Attack
705   BEM   Blade Element Momentum
706   CFD   Computational Fluid Dynamics
707   SST   Shear Stress Transport
708   TSR   Tip-Speed Ratio
709   U-RANS   Unsteady Reynolds-Averaged Navier-Stokes
710   VAWTs   Vertical Axis Wind Turbines
711
712   Greek symbols
713   α Angle of Attack (symbol)   [deg]
714   ϑ Azimuthal Angle   [deg]
715   π Dimensionless Pressure Coefficient   [-]
716   ω Specific Turbulence Dissipation Rate   [1/s]
717   Ω Turbine Revolution Speed   [rad/s]
718
719   Latin symbols
720   c Blade Chord   [m]
721   c_D Drag Coefficient   [-]
722   c_L Lift Coefficient   [-]
723   c_P Power Coefficient   [-]
724   c_T Torque Coefficient   [-]
725   D Rotor Diameter   [m]
726   F_D Drag Force   [N]
727   F_L Lift Force   [N]
728   k Turbulence Kinetic Energy   [m^2/s^2]
729   R Rotor Radius   [m]
730   Re Reynolds Number   [-]
731   Re_θ Momentum Thickness Reynolds Number   [-]
732   U Undisturbed Wind Speed   [m/s]
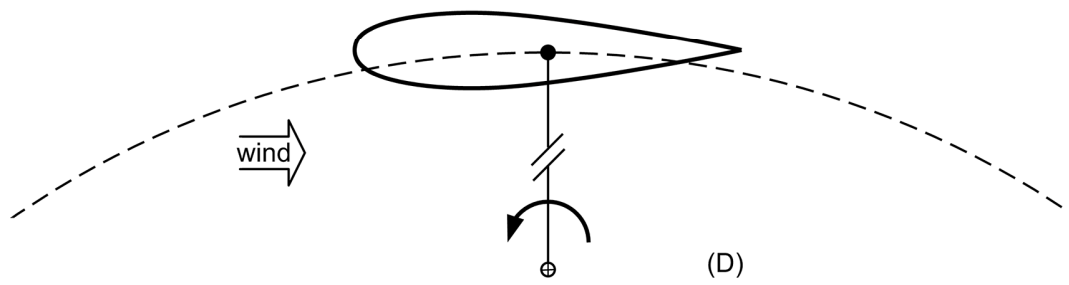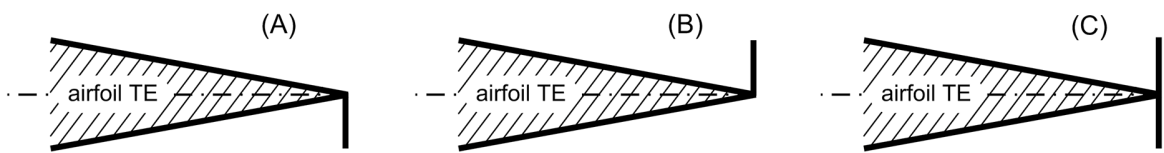733 w Relative Speed   [m/s]
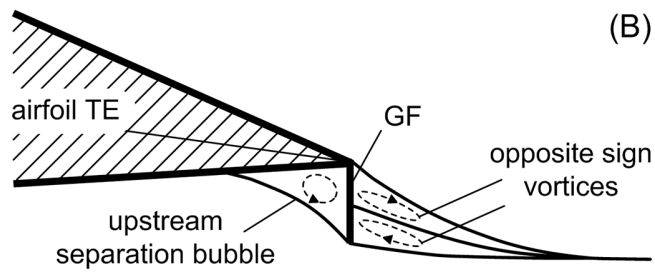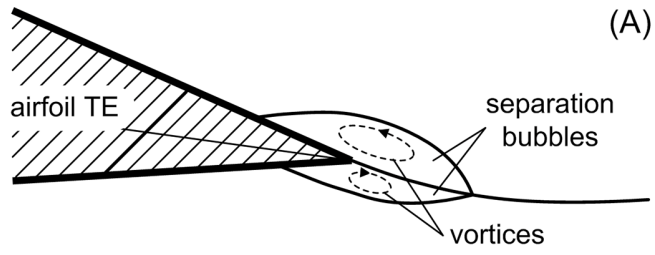734 y^+ Dimensionless Wall Distance   [-]
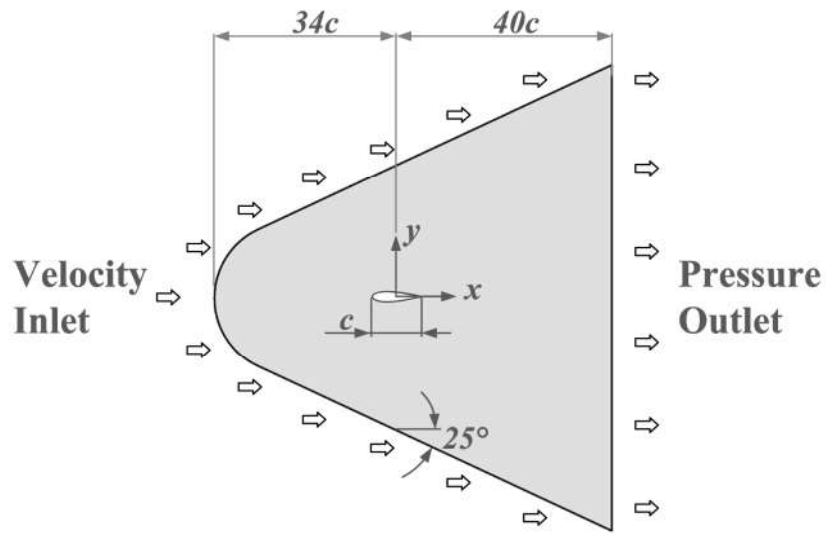

6. References

735
736 [1]   Cooper, P., 2010, "Development and analysis of vertical-axis wind turbines," *Wind Power
737   Generation and Wind Turbine Design*, ed. Wei Tong (Ashurst: WIT Press)
738 [2]   Damota, J., Lamas, I., Couce, A. and Rodríguez, J., 2015, "Vertical Axis Wind Turbines:
739   Current Technologies and Future Trends," *Proc. of the International Conference on

740   *Renewable Energies and Power Quality (ICREPQ'15)*, La Coruña (Spain), 25-27 March,
741   2015.

[3]   Sun, C., Lam, W.H., Cui, Y., Zhang, T., Jiang, J., Guo, J., Ma, Y., Wang, S., Tan, T.W., Chuah,
     J.H., Lam, S.S. and Hamill, G., 2018, "Empirical model for Darrieus-type tidal current turbine
     induced seabed scour," *Energy Conversion and Management*, 171, pp. 478-490.

[4]   Patel, V., Eldho, T.I. and Prabhu, S.V., 2017, "Experimental investigations on Darrieus straight
     blade turbine for tidal current application and parametric optimization for hydro farm
     arrangement," *International Journal of Marine Energy*, 17, pp. 110-135.

[5]   Bianchini, A., Ferrara, G., Ferrari, L., 2015, "Design guidelines for H-Darrieus wind turbines:
     Optimization of the annual energy yield," *Energy Conversion and Management*, 89(1 January
     2015), pp. 690-707

[6]   Arpino, F., Scungio, M., Cortellessa, G., 2018, "Numerical performance assessment of an
     innovative Darrieus-style vertical axis wind turbine with auxiliary straight blades," *Energy
     Conversion and Management*, 171(1 September 2018), pp. 769-777.

[7]   Wang, Y., Sun, X., Dong, X., Zhu, B., Zheng, Z., 2016, "Numerical investigation on
     aerodynamic performance of a novel vertical axis wind turbine with adaptive blades," *Energy
     Conversion and Management*, 108(15 January 2016), pp. 275-286.

[8]   Rezaeiha, A., Montazeri, H., Blocken, B., 2018, "Characterization of aerodynamic
     performance of vertical axis wind turbines: Impact of operational parameters," *Energy
     Conversion and Management*, 169(1 August 2018), pp. 45-77.

[9]   Ali, S., Lee, S.-M., Jang, C.-M., 2018, "Effects of instantaneous tangential velocity on the
     aerodynamic performance of an H-Darrieus wind turbine," *Energy Conversion and
     Management*, 171(1 September 2018), pp. 1322-1338.

[10]   Bianchini, A., Ferrara, G., Ferrari, L., 2015, "Pitch optimization in small-size Darrieus wind
     turbines," *Energy Procedia*, 81, pp. 122-132.

[11]   Ismail, F., Vihayaraghavan, K., 2013, CFD analysis of the effects of surface modification on
     a vertical turbine blade for improved aerodynamic flow control. *12th Americas Conference on
     Wind Engineering 2013 ACWE 2013: Wind Effects on Structures, Communities and Energy
     Generation*, 2, 1090-1096.

[12]   Liebeck, R. H., 1978, "Design of Subsonic Airfoils for High Lift", *J. Aircr.*, **15**(9), pp. 547–
     561.

[13]   Neuhart, D. H., and Pendergraft, O. C., 1988, "A Water Tunnel Study of Gurney Flaps", *Nasa
     Tech. Memo.*, **4071**(November), p. 22.

[14]   Storms, B. L., and Jang, C. S., 1994, "Lift Enhancement of an Airfoil Using a Gurney Flap and
     Vortex Generators", *J. Aircr.*, **31**(3), pp. 542–547.

[15]   Myose, R., Heron, I., and Papadakis, M., 1996, "Effect of Gurney Flaps on a NACA 0011
     Airfoil", *34th Aerospace Sciences Meeting and Exhibit*, American Institute of Aeronautics and
     Astronautics, Reston, VA, USA.

[16]   Myose, R., Heron, I., and Papadakis, M., 1996, "The Post-Stall Effect of Gurney Flaps on a
     NACA0011 Airfoil", *SAE Tech. Pap. 961316*.

[17]   Jang, C. S., Ross, J. C., and Cummings, R. M., 1998, "Numerical Investigation of an Airfoil
     with a Gurney Flap", *Aircr. Des.*, **1**(2), pp. 75–88.

[18]   Katz, J., and Dykstra, L., 1989, "Study of an Open-Wheel Racing-Car's Rear-Wing
     Aerodynamics", *SAE Tech. Pap. 890600*.

[19]   Li, Y., Wang, J., and Zhang, P., 2002, "Effects of Gurney Flaps on a NACA0012 Airfoil",
     Flow, Turbul. Combust., **68**(1), pp. 27–39.

[20]   Liu, T., and Montefort, J., 2007, "Thin-Airfoil Theoretical Interpretation for Gurney Flap Lift
     Enhancement", *J. Aircr.*, **44**(2), pp. 667–671.

[21]   Jeffrey, D., Zhang, X., and Hurst, D. W., 2001, "Some Aspects of the Aerodynamics of Gurney
     Flaps on a Double-Element Wing", *J. Fluids Eng.*, **123**(1), p. 99.

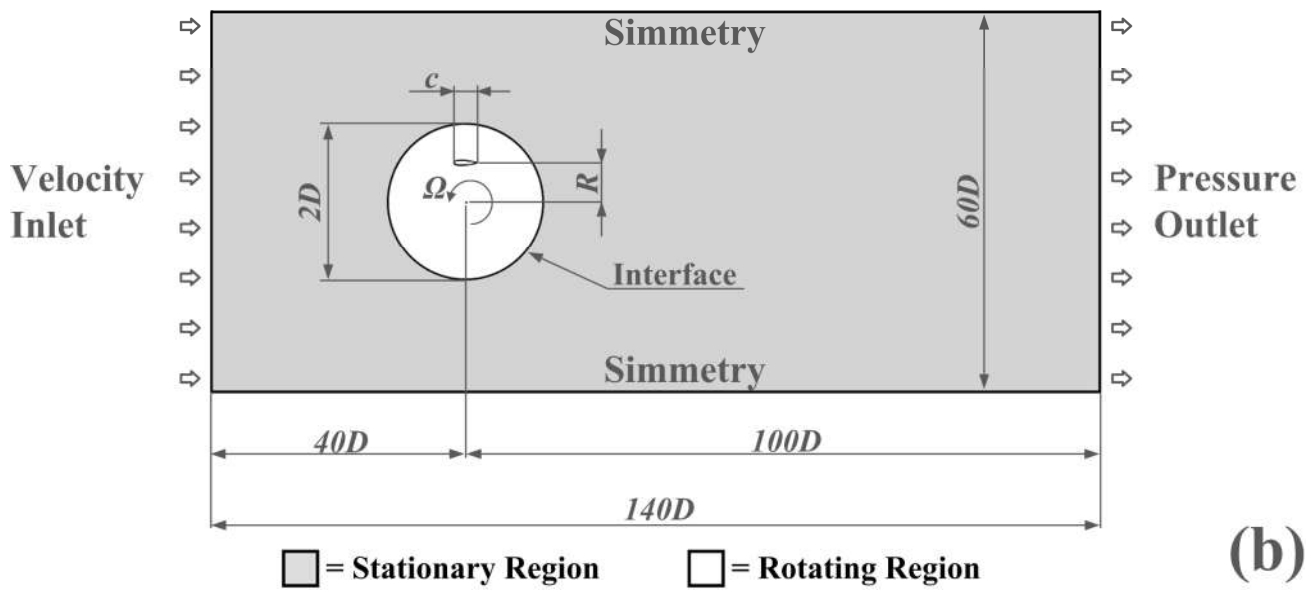[22]   Troolin, D. R., Longmire, E. K., and Lai, W. T., 2006, "Time Resolved PIV Analysis of Flow

over a NACA 0015 Airfoil with Gurney Flap", *Exp. Fluids*, **41**(2), pp. 241–254.

[23] Troolin, D. R., 2009, "A Quantitative Study of the Lift-Enhancing Flow Field Generated by an Airfoil with a Gurney Flap", University of Minnesota.

[24] Gopalakrishnan Meena, M., Taira, K., and Asai, K., 2018, "Airfoil-Wake Modification with Gurney Flap at Low Reynolds Number", *AIAA J.*, **56**(4), pp. 1348–1359.

[25] Brown, L., and Filippone, A., 2003, "Aerofoil at Low Speeds with Gurney Flaps", *Aeronaut. J.*, **107**(1075), pp. 539–546.

[26] Giguere, P., Lemay, J., and Dumas, G., 1995, "Gurney Flap Effects and Scaling for Low-Speed Airfoils", *13th Applied Aerodynamics Conference*, American Institute of Aeronautics and Astronautics, San Diego, CA, USA, p. 1881.

[27] Wang, J. J., Li, Y. C., and Choi, K.-S., 2008, "Gurney Flap—Lift Enhancement, Mechanisms and Applications", *Prog. Aerosp. Sci.*, **44**(1), pp. 22–47.

[28] Nilavarasan, T., Joshi, G.N., Chandel, S., 2018, "Aerodynamic performance characteristics of NACA 0010 cascade with Gurney Flaps," *International Journal of Turbo and Jet Engines*, article in press. DOI: 10.1515/tjj-2018-0012;

[29] Bae, E.S., Ghandi, F., 2012, "Upstream active Gurney Flap for rotorcraft vibration reduction," *Annual Forum Proceedings AHS International*, 2, 1354-1362.

[30] van Dam, C. P., Chow, R., Zayas, J. R., and Berg, D. E., 2007, "Computational Investigations of Small Deploying Tabs and Flaps for Aerodynamic Load Control", *J. Phys. Conf. Ser.*, **75**, p. 012027.

[31] Frederick, M., Kerrigan, E. C., and Graham, J. M. R., 2010, "Gust Alleviation Using Rapidly Deployed Trailing-Edge Flaps", *J. Wind Eng. Ind. Aerodyn.*, **98**(12), pp. 712–723.

[32] Pechlivanoglou, G., 2013, "Passive and Active Flow Control Solutions for Wind Turbine Blades", Technische Universität Berlin, Germany.

[33] Williams, T. J. H., 2014, "Compliant Flow Designs for Optimum Lift Control of Wind Turbine Rotors", University Of Notre Dame, IN, USA.

[34] Bach, A. B., 2016, "Gurney Flaps and Micro-Tabs for Load Control on Wind Turbines", Technische Universität Berlin, Germany.

[35] Pastrikakis, V., Woodgate, M., Barakos, G., 2017, "CFD method for modelling Gurney Flaps," Book Chapter in *Recent Progress in Flow Control for Pratical Flows: Results of the STADYWICO and IMESCON Projects*, 23-49. DOI: 10.1007/978-3-319-50568-8_2.

[36] Fuglsang, P., Bak, C., Gaunaa, M., and Antoniou, I., 2004, "Design and Verification of the Risø-B1 Airfoil Family for Wind Turbines", *J. Sol. Energy Eng.*, **126**(4), pp. 1002–1010.

[37] Tongchitpakdee, C., Benjanirat, S., and Sankar, L. N., 2006, "Numerical Studies of the Effects of Active and Passive Circulation Enhancement Concepts on Wind", *J. Sol. Energy Eng.*, **128**(4), pp. 432–444.

[38] Chen, H., and Qin, N., 2017, "Trailing-Edge Flow Control for Wind Turbine Performance and Load Control", *Renew. Energy*, **105**, pp. 419–435.

[39] Alber, J., Pechlivanoglou, G., Paschereit, C. O., Twele, J., and Weinzierl, G., 2017, "Parametric Investigation of Gurney Flaps for the Use on Wind Turbine Blades", *ASME Turbo Expo 2017: Turbomachinery Technical Conference and Exposition*, Charlotte, NC, USA., June 26–30, p. V009T49A015.

[40] Frunzulica, F., Dumitrescu, H., and Dumitrache, A., 2014, "Numerical Investigations of Dynamic Stall Control", *INCAS Bull. Spec. Issue*, **6**(1), pp. 67–80.

[41] Ismail, M. F., and Vijayaraghavan, K., 2015, "The Effects of Aerofoil Profile Modification on a Vertical Axis Wind Turbine Performance", *Energy*, **80**, pp. 20–31.

[42] Balduzzi F, Bianchini A, Ferrari L, et al. Static and dynamic analysis of a NACA 0021 airfoil section at low Reynolds numbers based on experiments and CFD. ASME. *J. Eng. Gas Turbines Power.* 2018;141(5):. doi:10.1115/1.4041150.

[43] Barlow, J.B., Rae Jr., W.H. and Pope, A., 1999, *Low-speed Wind Tunnel Testing*, Wiley-Interscience Publication, New York, USA.

842 [44] Dossena, V., Persico, G., Paradiso, B., Battisti, L., Dell'Anna, S., Brighenti, A., and Benini,
843 E., 2015, "An Experimental Study of the Aerodynamics and Performance of a Vertical Axis
844 Wind Turbine in a Confined and Unconfined Environment", *J. Energy Resour. Technol.*,
845 **137**(5), p. 051207.
846 [45] Balduzzi, F., Bianchini, A., Gigante, F. A., Ferrara, G., Campobasso, M. S., and Ferrari, L.,
847 2015, "Parametric and Comparative Assessment of Navier-Stokes CFD Methodologies for
848 Darrieus Wind Turbine Performance Analysis", *Proceedings of the ASME Turbo Expo 2015:*
849 *Turbine Technical Conference and Exposition*, Montreal, QC, Canada, June 15–19, p.
850 V009T46A011.
851 [46] Bianchini, A., Balduzzi, F., Ferrara, G., and Ferrari, L., 2016, "Aerodynamics of Darrieus
852 Wind Turbines Airfoils: The Impact of Pitching Moment", *J. Eng. Gas Turbines Power*,
853 **139**(4), p. 042602.
854 [47] Bianchini, A., Balduzzi, F., Ferrara, G., and Ferrari, L., 2016, "Influence of the Blade-Spoke
855 Connection Point on the Aerodynamic Performance of Darrieus Wind Turbines", *ASME Turbo*
856 *Expo 2016: Turbomachinery Technical Conference and Exposition*, Seoul, South Korea, June
857 13–17, p. V009T46A012.
858 [48] Balduzzi, F., Drofelnik, J., Bianchini, A., Ferrara, G., Ferrari, L., and Campobasso, M. S.,
859 2017, "Darrieus Wind Turbine Blade Unsteady Aerodynamics: A Three-Dimensional Navier-
860 Stokes CFD Assessment", *Energy*, **128**, pp. 550–563.
861 [49] Balduzzi, F., Marten, D., Bianchini, A., Drofelnik, J., Ferrari, L., Campobasso, M. S.,
862 Pechlivanoglou, G., Nayeri, C. N., Ferrara, G., and Paschereit, C. O., 2017, "Three-
863 Dimensional Aerodynamic Analysis of a Darrieus Wind Turbine Blade Using Computational
864 Fluid Dynamics and Lifting Line Theory", *J. Eng. Gas Turbines Power*, **140**(2), p. 022602.
865 [50] Bianchini, A., Balduzzi, F., Ferrara, G., and Ferrari, L., 2016, "Virtual Incidence Effect on
866 Rotating Airfoils in Darrieus Wind Turbines", *Energy Convers. Manag.*, **111**, pp. 329–338.
867 [51] Balduzzi, F., Bianchini, A., Ferrara, G., and Ferrari, L., 2016, "Dimensionless Numbers for the
868 Assessment of Mesh and Timestep Requirements in CFD Simulations of Darrieus Wind
869 Turbines", *Energy*, **97**, pp. 246–261.
870 [52] Rainbird, J. M., Bianchini, A., Balduzzi, F., Peiró, J., R. Graham, J. M., Ferrara, G., and Ferrari,
871 L., 2015, "On the Influence of Virtual Camber Effect on Airfoil Polars for Use in Simulations
872 of Darrieus Wind Turbines", *Energy Convers. Manag.*, **106**, pp. 373–384.
873 [53] Maître, T., Amet, E., and Pellone, C., 2013, "Modeling of the Flow in a Darrieus Water
874 Turbine: Wall Grid Refinement Analysis and Comparison with Experiments", *Renew. Energy*,
875 **51**, pp. 497–512.
876 [54] Raciti Castelli, M., Englaro, A., and Benini, E., 2011, "The Darrieus Wind Turbine: Proposal
877 for a New Performance Prediction Model Based on CFD", *Energy*, **36**(8), pp. 4919–4934.
878 [55] Balduzzi, F., Bianchini, A., Maleci, R., Ferrara, G., and Ferrari, L., 2016, "Critical Issues in
879 the CFD Simulation of Darrieus Wind Turbines", *Renew. Energy*, **85**, pp. 419–435.
880 [56] *ANSYS® Fluent®, ©2015 ANSYS, Inc., Release 16.1.0.*
881 [57] Menter, F. R., 1994, "Two-Equation Eddy-Viscosity Turbulence Models for Engineering
882 Applications", *AIAA J.*, **32**(8), pp. 1598–1605.
883 [58] Marten, D., Wendler, J., Pechlivanoglou, G., Nayeri, C. N., and Paschereit, C. O., 2013,
884 "QBlade: An Open Source Tool for Design and Simulation of Horizontal and Vertical Axis
885 Wind Turbines", *Int. J. Emerg. Technol. Adv. Eng.*, **3**(3), pp. 264–269.
886 [59] Bianchini, A., Balduzzi, F., Ferrara, G., Ferrari, L., Persico, B., Dossena, V. and Battisti, L.,
887 2017, "Detailed analysis of the wake structure of a straight-blade H-Darrieus wind turbine by
888 means of wind tunnel experiments and CFD simulations," *J. Eng. Gas Turbines Power*, **140**(3),
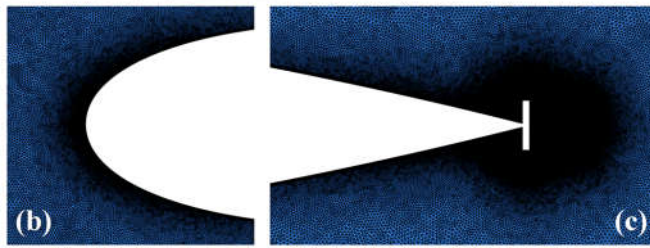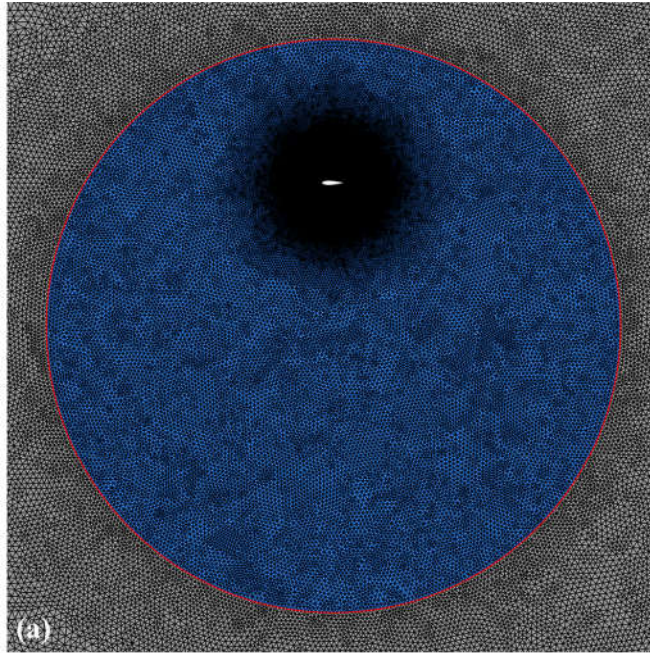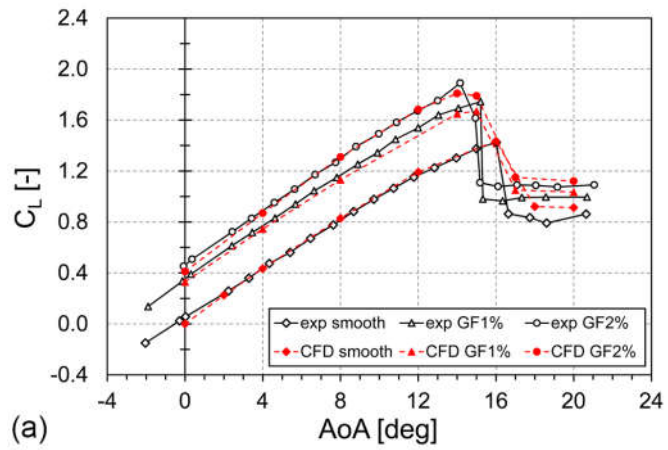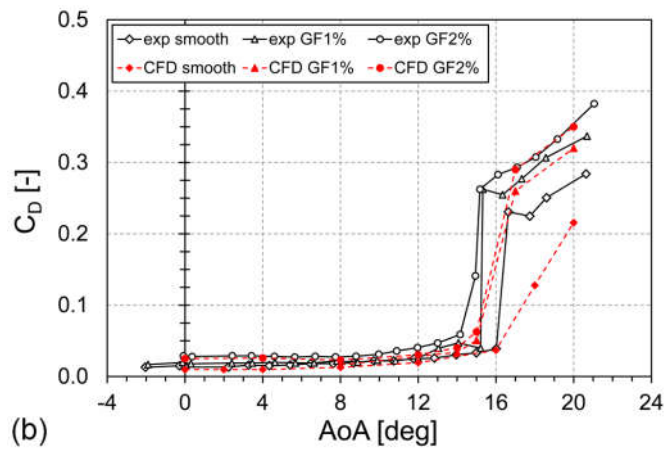889 pp. 032604-032604-9.
890

(A)

airfoil TE

separation
bubbles

vortices

(B)

airfoil TE

GF

opposite sign
vortices

upstream
separation bubble

(A)

airfoil TE

(B)

airfoil TE

(C)

airfoil TE

wind

(D)

(a)

(b)

(a)

(b)

(c)

(a)

(b)

(a)

(b)

Baseline smooth

GFin

GFout

GFboth

ω^* [-]

45.0
39.0
33.0
27.0
21.0
15.0
9.0
3.0
-3.0
-9.0
-15.0
-21.0
-27.0
-33.0
-39.0
-45.0

Baseline smooth
GF in 2%c
GF out 2%c
GF both 2%c

π [-]

x/c [-]

Baseline smooth
GFin 3%c
GFout 3%c
GFboth 3%c

c_P [-]

TSR [-]